Characterization of the Tyrosine-Z Radical and Its Environment in the Spin-Coupled $S_2Tyr_Z^\bullet$ State of Photosystem II from *Thermosynechococcus elongatus*†

Sun Un,*,‡ Alain Boussac,‡ and Miwa Sugiura§

Service de Bioénergétique, URA CNRS 2096, DBJC, CEA Saclay, 91191 Gif sur Yvette, France, and Department of Plant Biosciences, School of Life and Environmental Sciences, Osaka Prefecture University, 1-1 Gakuen-cho, Naka-ku, Sakai, Osaka 599-8531, Japan

Received October 6, 2006; Revised Manuscript Received January 10, 2007

ABSTRACT: The Mn_4Ca cluster of photosystem II (PSII) goes through five sequential oxidation states (S_0−S_4) in the water oxidation process that also involves a tyrosine radical intermediate ($Tyr_Z^\bullet$). An $S_2Tyr_Z^\bullet$ state in which the Mn_4Ca cluster and $Tyr_Z^\bullet$ are magnetically coupled to each other and which is characterized by a distinct "split-signal" EPR spectrum can be generated in acetate-treated PSII. This state was examined by high-field EPR (HFEPR) in PSII from *Thermosynechococcus elongatus* isolated from a D2-Tyr160Phe mutant to avoid spectral contributions from $Tyr_D^\bullet$. In contrast to the same state in plants, both antiferromagnetic and ferromagnetic spin−spin couplings were observed. The intrinsic g values of $Tyr_Z^\bullet$ in the coupled state were directly measured from the microwave frequency dependence of the HFEPR spectrum. The $Tyr_Z^\bullet$ g_x value in the antiferromagnetic centers was 2.0083, indicating that the coupled radical was in a less electropositive environment than in Mn-depleted PSII. Two g_x values were found in the ferromagnetically coupled centers, 2.0069 and 2.0079. To put these values in perspective, the second redox-active tyrosine, $Tyr_D^\bullet$, was examined in various electrostatic environments. The $Tyr_D^\bullet$ g_x value changed from 2.0076 in the wild type to 2.0095 when the hydrogen bond from histidine 189 to $Tyr_D^\bullet$ was removed using the D2-His189Leu mutant, indicating a change to a significantly less electropositive environment. BLY3P/6-31+G** density functional calculations on the hydrogen-bonded *p*-ethylphenoxy radical−imidazole supermolecular model complex showed that the entire range of $Tyr^\bullet$ g_x values, from 2.0065 to 2.0095, could be explained by the combined effects of hydrogen bonding and the dielectric constant of the local protein environment.

Photosystem II (PSII)[1] is the enzyme responsible for oxygen evolution. The evolution of oxygen as a result of light-driven water oxidation is catalyzed by a Mn_4Ca cluster which acts both as a device for accumulating oxidizing equivalents and as the active site. Absorption of a photon induces a charge separation which results in the oxidation of a chlorophyll molecule (P_{680}) and the reduction of a pheophytin molecule. The pheophytin anion transfers the electron to a quinone, Q_A, and P_{680}^+ is reduced by a tyrosine residue of the D1 polypeptide, Tyr_Z, which in turn is reduced by the Mn_4Ca cluster. Although a number of recent reviews have put forward various hypotheses regarding how water is oxidized and oxygen evolves (*1*−*7*), fundamental aspects of the mechanism of O_2 evolution remain to be elucidated.

The relative arrangement of the important cofactors has been known for some time from various different comparative studies and spectroscopic measurements (*8*). More recently, their absolute physical positions within the protein have been determined from crystal structures. The structure of PSII isolated from the thermophilic cyanobacterium *Thermosynechococcus elongatus* has been determined to 3.5 and 3.0 Å resolution (*9*, *10*). However, the crystallographically determined structures are not without problems. For example, the structure of the Mn_4Ca cluster is still under debate since its redox state is undefined in the crystallographic structures due to the reductive effect of the X-rays that were used (*11*, *12*). More fundamentally, crystallographic structures by themselves, especially at their current modest resolution, tell us very little about the various important protein−cofactor and cofactor−cofactor interactions that influence the electronic properties of the cofactors and the enzyme function. However, via combination of the detailed physical structure obtained from crystallography with the electronic structural information from spectroscopy, a more precise functional picture of structure can be obtained.

In this respect, PSII isolated from *T. elongatus* provides an ideal framework. The protein itself is very robust (*13*). The genomic sequence of the organism has been determined

† A.B. and M.S. thank the JSPS and CNRS under the Japan-France Research Co-operative Program for funding.

* To whom correspondence should be addressed. E-mail: sun@herode.saclay.cea.fr. Fax: 33 (0)1 69 08 87 17. Tel: 33 (0)1 69 08 28 42.

‡ CEA Saclay.

§ Osaka Prefecture University.

[1] Abbreviations: PSII, photosystem II; WT′, His_6-tagged photosystem II from *T. elongatus*; EPR, electron paramagnetic resonance; HFEPR, high-field EPR; Tris, tris(hydroxymethyl)aminomethane; MES, 2-morpholinoethanesulfonic acid.

10.1021/bi062084f CCC: $37.00
Published on Web 02/27/2007

(*14*), and molecular biological technologies are well under development. For example, a His_6-tagged variant of *T. elongatus* PSII has been created that greatly facilitates protein isolation (*13*). We have shown that this variant, which we will call WT′, is very well-suited for EPR experiments (*15*). In this work, we have expanded these previous studies. We have manipulated the stable tyrosyl radical (Tyr160), $Tyr_D^\bullet$, and its environment, both to study the impact of the protein environment on the electronic structure of Tyr_D and to remove this stable radical so that its companion tyrosyl radical $Tyr_Z^\bullet$ could be examined in detail without the spectroscopic interference from $Tyr_D^\bullet$ (*16*).

During the enzyme cycle, the oxidizing side of PSII goes through five sequential redox states, denoted S_n where n varies from 0 to 4. Oxygen is released during the S_3 to S_0 transition in which S_4 is a transient state. When either Ca^{2+} or Cl^-, each an essential cofactor for O_2 evolution, is removed from its site, manganese oxidation can still take place, allowing the formation of the S_2 state, but in the following step, the normal S_3 state is not formed (*17*, *18*). Instead, an alternate abnormally stable form appears to be induced. This state is thought to be one in which the metal cluster is in the S_2 state and a nearby radical (*17*, *18*), the tyrosine residue $Tyr_Z^\bullet$ (*19*), has been formed. In this state, the Mn_4Ca cluster ($S = {}^1/_2$) and $Tyr_Z^\bullet$ ($S = {}^1/_2$) magnetically interact, giving rise to a characteristic EPR resonance that is known as the split signal (*17*, *18*) due to its doublet structure (see also ref *20*).

Several other split signals have now been observed in functional PSII. All have been generated at liquid helium temperatures by illuminating PSII either in the S_0 and S_1 states with visible light or in the S_3 state with infrared light. The species that are formed under these conditions have been proposed to correspond to "nonrelaxed" $S_0Tyr_Z^\bullet$, $S_1Tyr_Z^\bullet$, and $S_2Tyr_Z^\bullet$ states (*21*−*24*). Since the room-temperature lifetimes of these three states are very short, it has not been possible to trap and study them at low temperatures. Thus, the relevance of these states to normal enzyme chemistry has yet to be established. Nevertheless, several pieces of information have led the authors to propose that they correspond to functional intermediate states. Therefore, it is apparent that a detailed understanding of these spin-coupled states will be important to understanding the enzyme chemistry. To this end, we have examined the HFEPR spectra of the $S_2Tyr_Z^\bullet$ spin-coupled state in the acetate-treated D2-Tyr160Phe mutant not only to characterize the spin−spin interaction but also to learn more about the electronic state of the tyrosyl radical by measuring its intrinsic g values. To do this, we coupled the normal field-swept spectroscopy with a multifrequency approach that allowed us to directly measure the g values of the radical.

The theory regarding the EPR spectroscopy of the $S_2Tyr^\bullet$ split signal has been previously discussed (*25*−*30*). The analyses of our measurements were based on the spin Hamiltonian

$$H = \beta\vec{S}_R\cdot g_R\cdot\vec{B} + \beta\vec{S}_M\cdot g_M\cdot\vec{B} + \vec{S}_M\cdot\sum_i A_i\cdot\vec{I}_i + \vec{S}_R\cdot C\cdot\vec{S}_M \quad (1)$$

where the subscripts M and R refer to the metal center and tyrosyl radical, respectively. The first two terms are the Zeeman interactions of the radical and manganese cluster, respectively; the third is the four hyperfine interactions internal to the manganese cluster, and the last term is the general symmetric spin−spin coupling between the two spins. The isotropic and anisotropic parts of the coupling correspond to the exchange and dipolar interactions, respectively. When the applied magnetic-field is sufficiently large that Zeeman interaction dominated, one effect of the spin−spin interaction is to displace the resonance of the radical from its intrinsic field position, defined by g_R. When displacement is to a lower magnetic field (or to apparently higher g values), the spin−spin coupling value is greater than zero or antiferromagnetic. For displacement to a higher magnetic field, the coupling is less than zero and ferromagnetic. The theoretical details underlying our measurements are presented in the Appendix.

MATERIALS AND METHODS

Construction of Mutants. Construction of the His_6-tagged *T. elongatus* strain (hereafter called WT′) and that of the His_6-tagged D2-Tyr160Phe PSII mutant have been described previously (*13*, *16*), The His189Leu mutation in the D2 protein was constructed in the *psbD*$_1$ gene into a host strain of *T. elongatus* lacking the *psbD*$_2$ gene (strain Δ*psbD*$_2$) (*16*). The His to Leu mutation at position 189 in the D2 protein was introduced together with the hexahistidine tag on the carboxy terminus of CP43 with the following procedure. The mutation-bearing plasmid was constructed by PCR amplification using the forward primer (5′-CTTTTTCCAAGGGTTttaAACTGGACCTTGAACCCC-3′) and the reverse primer (5′-GGGGTTCAAGGTCCAGTTtaaaAACCCTTGGAAAAAG-3′) for changing D2-His189 to D2-Leu189 and for producing restriction recognition site *Dra*I (underlined bases) in the same amount of time (the lowercase characters correspond to bases changed in the mutation). The Δ*psbD*$_2$ *T. elongatus* cells were then transformed with this plasmid, and single colonies were selected for their ability to grow on solid DTN media containing 40 μg/mL kanamycin monosulfate and 5 μg/mL chloramphenicol as described previously (*13*, *16*). To confirm the complete segregation of the strain, the nucleotides of the genome were amplified using primers corresponding to positions −35 to −5 and 630−660 of *psbD*$_1$. The resulting amplified 695 bp DNA was analyzed after digestion with *Dra*I (New England Biolabs).

PSII Purification. WT′ cells and mutant cells were grown in 3 L Erlenmeyer flasks (1 L culture) in a rotary shaker (120 rpm) at 45 °C under continuous illumination with fluorescent white lamps (≈80 μmol of photons m^{-2} s^{-1}) in a CO_2-enriched atmosphere. PSII was purified exactly as previously described (*13*, *16*) and was stored in liquid nitrogen until it was used at a concentration of ≈2 mg of Chl/mL in a medium containing 10% glycerol, 1 M betaine, 15 mM $CaCl_2$, 15 mM $MgCl_2$, and 40 mM MES (pH 6.5). The oxygen evolution activity of PSII isolated from the three strains and measured under saturating light conditions with 2,6-dichloro-1,4-benzoquinone (DCBQ) as an electron acceptor varied from 3500 to 4200 μmol of O_2 (mg of Chl)$^{-1}$ h^{-1} from batch to batch. DCBQ reacts in the minute time range with betaine in the presence of O_2, forming some quinol and probably semiquinone and superoxide anions (not shown). For that reason, measurements of PSII activity should be taken very shortly after the addition of DCBQ.

Acetate Treatment. The split signal was generated in acetate-treated PSII (*31*, *32*). For the acetate treatment, PSII samples were diluted approximately 10 times in a medium containing 0.3 M mannitol, 1 M betaine, 15 mM $Ca(OH)_2$, and MES to adjust the pH to 6.5. The samples were collected by centrifugation (15 min at 170000*g*) after the addition of the same medium containing 50% (w/v) polyethylene glycol 8000 so that the final PEG concentration in the PSII suspension was 12%. After centrifugation, the pellet was resuspended in a medium containing 0.5 M acetic acid, 0.3 M mannitol, 1 M betaine, 15 mM $Ca(OH)_2$, and 40 mM MES (pH 5.2) (the pH was previously adjusted by adding NaOH). Then, the samples were collected by centrifugation (15 min at 170000*g*) after the addition of the same medium containing 50% (w/v) polyethylene glycol 8000 so that the final PEG concentration was 12%. The final pellet was resuspended in 0.5 M acetate, 0.3 M mannitol, 1 M betaine, 15 mM $Ca(OH)_2$, and 40 mM MES (pH 5.2) and loaded into EPR tubes.

Formation of the Split Signal in the D2-Tyr160Phe PSII Mutant. Immediately after the acetate treatment, the sample was dark-adapted for 30 min at room temperature, and 1 mM phenyl-*p*-benzoquinone dissolved in dimethyl sulfoxide was then added to the sample as an exogenous electron acceptor. Formation of the split signal was achieved by room-temperature illumination of the samples with 18 laser flashes (500 ms apart, 532 nm, 550 mJ, 8 ns Spectra Physics GCR-230-10). Then, the sample was immediately frozen at 200 K in a bath containing ethanol and dry ice and cooled to 77 K in liquid nitrogen.

Manganese Depletion. PSII samples were diluted approximately 10-fold in a medium containing 1.2 M Tris-HCl (pH 9.2) and were incubated under room light at 4 °C for 1 h. The samples were collected by centrifugation (15 min at 170000*g*) after the addition of 1.2 M Tris (pH 9.2) containing 50% (w/v) polyethylene glycol 8000 so that the final PEG concentration was 12%. The final pellet was resuspended in a medium containing 0.3 M mannitol and 100 mM NaCl buffered with either 50 mM Tris (pH 8.5), 50 mM MES (pH 6.5), or 50 mM CAPS (pH 10) or in the acetate buffer at pH 5.5 described above. Generation of $Tyr_Z^\bullet$ and $Tyr_D^\bullet$ in the various Mn-depleted PSII was carried out as described in Results. Unless indicated otherwise, the samples were illuminated using a 1000 W tungsten lamp filtered with water and filters to minimize the level of infrared radiation.

EPR Measurements. CW-EPR 9 GHz spectra were recorded at liquid helium temperatures with a Bruker ESP300 spectrometer equipped with an Oxford Instruments cryostat. The HFEPR measurements were taken on a locally built spectrometer described previously (*33*). Using a Mn-doped magnesium oxide sample, we verified that the relative accuracy of the magnetic field was better than 1×10^{-3} T over the field ranges used in this study. The microwave frequency was accurate to better than 1 MHz. Hence, the measurement accuracy in *g* was expected to be 1×10^{-4}. In practice, the accuracy was limited by the broadness of the resonances. The measurements were analyzed using XMGRACE (http://plasma-gate.weizmann.ac.il/Grace). In most cases, six sharp resonances arising from adventitious Mn(II) ions were observed. In some cases, they were subtracted from the spectra by first isolating one of the resonances and using it to generate a six-line spectrum by Fourier convolution. Visual inspection indicated that such a suppression procedure was adequate. As will be seen (see below), the region of the 285 GHz HFEPR spectrum centered around 10.21 T exhibited complete suppression of the Mn(II) resonance. In the high-field cryogenic photo-oxidation experiments, a small 10 mW green laser was used to illuminate the samples directly inside the magnet.

Density Functional Calculations. Density functional calculations were carried out with Gaussian 03 (revision B.05) (*34*). The B3LYP hybrid density functional (*35*−*37*) and 6-31+G(D,P) basis set were used for geometry optimization and subsequent calculation of *g* values. Frequency calculations were performed to ensure the geometry optimization calculations were true potential minima. The *g* value calculation in Gaussian 03 uses the method similar to that of Neese (*38*), but instead uses gauge-independent atomic orbitals (GIAO) (*39*). Calculations of solvent effects were carried out using the polarizable continuum (PCM) model implemented in Gaussian 03. The default solvent parameters that were available within the package were used. In particular, benzene ($\epsilon = 2.247$ D), chloroform ($\epsilon = 4.9$ D), dichloroethane ($\epsilon = 10.36$ D), acetone ($\epsilon = 20.7$ D), and methanol ($\epsilon = 32.63$ D) were used.

RESULTS

In the presence of acetate, the S state cycle is blocked after formation of the $S_2Tyr_Z^\bullet$ state. In this inhibited state, the Mn_4Ca cluster and $Tyr_Z^\bullet$ are magnetically coupled to each other and a characteristic split signal can be detected by EPR. The split signal in acetate-treated D2-Tyr160Phe-PSII is shown in Figure 1. Spectrum a was recorded on a dark-adapted sample (i.e., in the S_1 state), and spectrum b was recorded after flash illumination at room temperature (i.e., with $S_2Tyr_Z^\bullet$ in the majority of centers). Spectrum c corresponds to the light-minus-dark spectrum (with an expanded magnetic field scale). As previously demonstrated in this mutant (*16*), the central part of the $S_2Tyr_Z^\bullet$ split signal could be readily detected in the light-minus-dark spectrum (spectrum c) since there was no interference from the $Tyr_D^\bullet$ radical that is normally present in the WT′ spectra.

Figure 2 shows the 4.2 K, 285 GHz EPR spectrum of the split signal in acetate-treated D2-Tyr160Phe-PSII (black trace). This signal was different in a number of ways from the HFEPR spectra previously reported by us (*30*). First and foremost in the 9 GHz spectrum was the absence of the obscuring $Tyr_D^\bullet$ resonances (Figure 2, red trace). Instead, a sharp, but low-intensity, resonance originating from a chlorophyll cation was detected in the center of the spectrum (approximately at $g = 2.002$). This resonance was previously characterized but, in this case, did not contribute significantly to the 9 GHz spectrum because it was largely saturated due to the high microwave power (Figure 1) (*16*). The portion of the HFEPR spectrum above the free electron *g* value ($g_{free} = 2.002326$) looked very similar to that of the split signal in acetate-treated PSII from spinach (*30*). The two lowest field resonances, at 10.14 and 10.15 T, had exact correspondences in the spinach spectrum (Figure 2, green trace). The *T. elongatus* spectrum also had a very broad feature below g_{free} somewhat similar to that found in calcium-depleted PSII from spinach (Figure 2, blue trace), although it was much broader in the former. This broad resonance

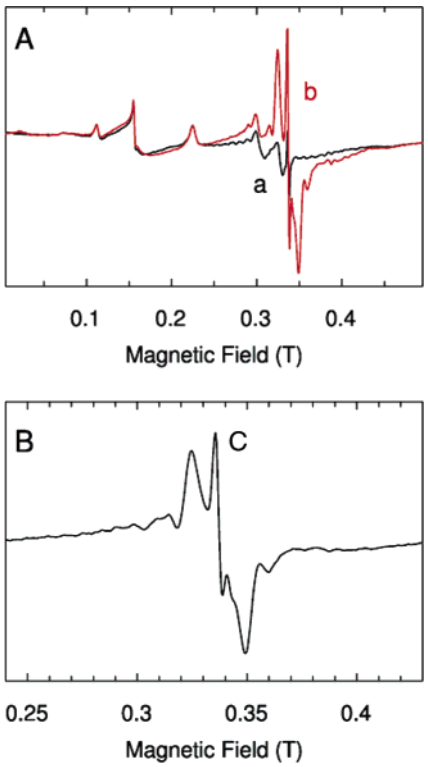

FIGURE 1: EPR spectra (9 GHz) in acetate-treated D2-Tyr160Phe-PSII. Spectrum a is the EPR spectrum of dark-adapted (S_1 state) and spectrum b is after 18 laser flashes at room temperature. Instrument settings: modulation amplitude, 18 G; microwave power, 20 mW; microwave frequency, 9.4 GHz; modulation frequency, 100 kHz; and temperature, 9 K. The chlorophyll concentration was ~2 mg/mL. Spectrum c is the difference of spectrum b minus spectrum a.

was not the manganese cluster counterpart of the split signal which in principle must also have been present. To date, we have been unsuccessful in our attempts to detect the S_2 "multiline" signal. Hence, it seemed highly unlikely that we could do so in the $S_2Tyr_Z^\bullet$ experiments. This broad component also did not come from the lower $m_s = -5/2 \rightarrow -3/2$ or $m_s = -3/2 \rightarrow -1/2$ transitions of adventitious Mn(II) since its amplitude did not correlate from sample to sample with the amplitude of the six much sharper $m_s = -1/2 \rightarrow 1/2$ transitions that were also readily detectable (see below). Moreover, resonances from these lower Mn(II) transitions should also have had contributions below g_{free} for which there was no evidence. The energy-level diagrams in Figure 2 show the correspondence between the transitions, ΔE_{Tyr}, and observed resonances when the spin−spin interaction, C, is positive (green arrows) and negative (blue arrows). A more complete explanation of the diagram has been provided by Dorlet and co-workers (*30*).

Under the high-magnetic field and low-temperature conditions used to obtain the spectrum in Figure 2, only half of the "doublet" structure that characterizes the conventional 9 GHz spectrum was expected to be detected with the sign of the spin−spin interaction dictating which half was observed (*30*). The green and blue arrows in the energy diagrams in Figure 2 denote the corresponding transitions. Since there was spectral intensity above and below g_{free}, it was concluded that the sample contained centers with positive (above g_{free}) spin−spin interactions and others with a negative (below g_{free}) value. The position and broadness of the high-field edge of the spectrum suggested that the latter negative spin−spin interactions were stronger and likely to be highly distributed.

The two different centers could be further distinguished by their distinct temperature dependencies. The changes could be best seen in the integrated EPR spectra. Figure 3 shows the integral of HFEPR spectra of the split signal recorded at temperatures ranging from 4 to 88 K. Except for the anticipated reduction in global spectral intensity, there was little change from 4 to 10 K. The excess intensity in the 10 K spectrum could be traced to the increasing intensity of the remaining half of the doublet structure that is not seen at 4 K that occurs as the $S_2Tyr_Z^\bullet$ spin states become more equally populated with an increase in temperature (see ref *30* for details). The sharp adventitious Mn(II) lines provided a good reference for comparing intensities at higher temperatures. Four of the six resonances from the $m_s = -1/2 \rightarrow 1/2$ transition Mn(II) ions were clearly resolved at 10.17, 10.197, 10.207, and 10.217 T. The magnitudes of these resonances sharply rose from 4 K to a maximum at ~20 K and then fell slowly from 20 to 80 K to approximately one-third of the maximum intensity as theoretically predicted. When the spectra obtained above 10 K were scaled so that the Mn(II) lines were approximately the same (Figure 3), it became readily apparent that spectral intensity above and below sharp chlorophyll cation resonance behaved very differently. Beyond 25 K, the spectral intensity at magnetic fields above the chlorophyll cation signal dropped off much faster than the Mn(II) resonance, so much so that at 88 K very little intensity remained. This loss in the high-field intensity was not offset by the appearance of additional intensity elsewhere. By comparison, with the exception of the initial loss in resolution, the low-field portion of the spectra remained unchanged with an increase in temperature and was present even at 88 K. The approximately constant width and shape of the low-field region indicated that the phenomenon of exchange narrowing (*40*) was not significant up to 90 K. The asymmetric behavior also ruled out the contributions from Mn(II) transitions other than the $m_s = -1/2 \rightarrow 1/2$ transition. For example, the spectral intensity from the broad $m_s = -5/2 \rightarrow 3/2$ and $m_s = 3/2 \rightarrow 5/2$ transitions will tend to equalize, making the Mn(II) spectrum more symmetric, as the six electronic spin states become more equally populated with an increase in temperature. Hence, the temperature dependence of the HFEPR spectra strongly reinforced the notion that there were two distinct populations of spin-coupled $S_2Tyr_Z^\bullet$ centers.

Previous temperature dependence studies (*31*, *32*) carried out at 9 GHz on PSII from spinach reported the disappearance of the split signal at high temperatures and the appearance of a simple tyrosyl radical spectrum due to exchange narrowing. The detection of the split signal at 285 GHz at temperatures close to 88 K (see Figure 3) was inconsistent with these earlier observations. Therefore, the temperature dependence of the 9 GHz EPR spectra of the acetate-treated PSII was investigated in the same D2-Tyr160Phe-PSII that was used for HFEPR measurements (Figure 4). In Figure 4A, the spectra of the split signal recorded between 4 and 116 K are shown. As previously reported (*31*, *32*), increasing the temperature resulted in a narrowing of the signal above approximately 15 K and then to its total disappearance above 100 K. This behavior, although slightly different from that observed in the HFEPR spectra, was not

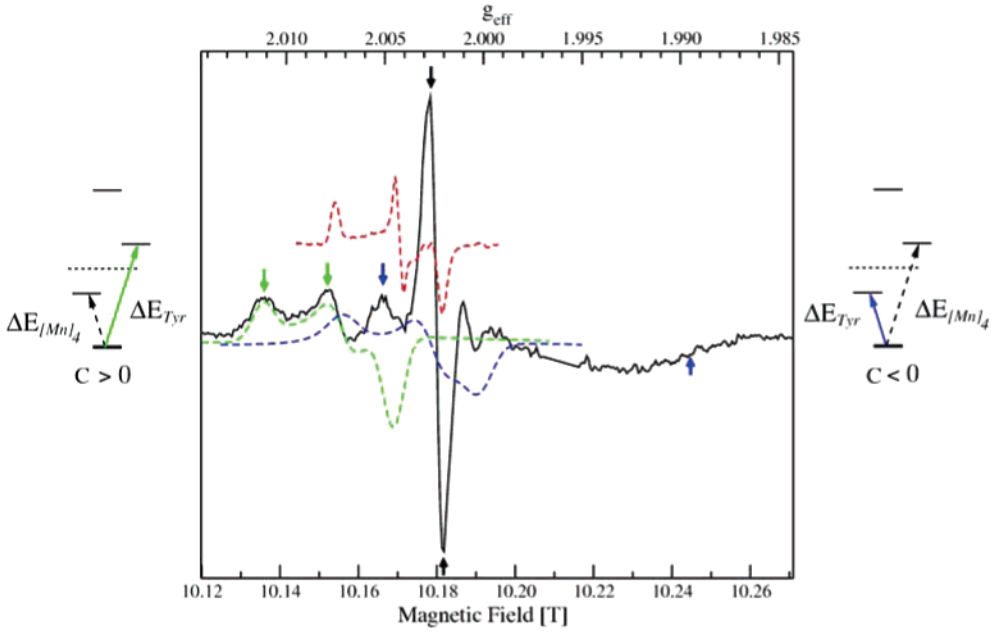

FIGURE 2: Split signal (285 GHz) from acetate-treated D2-Tyr160Phe-PSII from *T. elongatus* recorded at 4 K (black). For comparison, a native $Tyr_D^{\bullet}$ obtained from a WT′ sample is shown in red. The 4 K simulations of the signal from acetate-treated (green) and calcium-depleted (blue) PSII samples from spinach are also shown (see ref *30* for details). The six arrows indicate the features that were monitored in the field frequency measurements. The energy-level diagrams show the correspondence between the transitions, ΔE_{Tyr}, and observed resonances when the spin−spin interaction, Λ, is positive (green arrows) and negative (blue arrows). All spectra have been arbitrarily scaled.

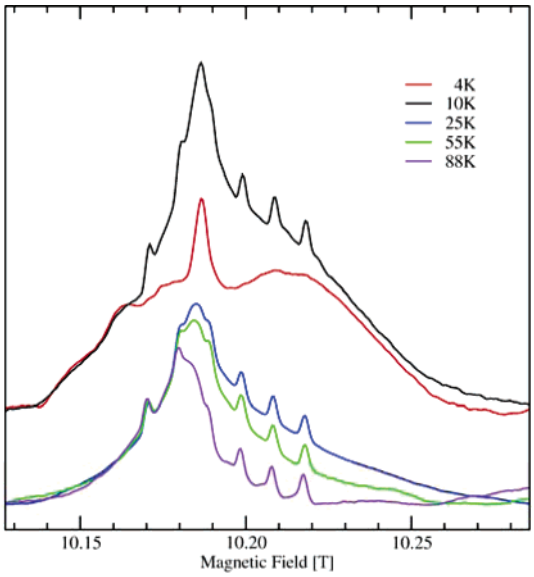

FIGURE 3: Temperature dependence of the light-induced split signal in acetate-treated D2-Tyr160Phe-PSII from *T. elongatus*. The spectra have been arbitrarily scaled in amplitude to facilitate comparison. The six relatively sharp features are due to adventitious Mn(II).

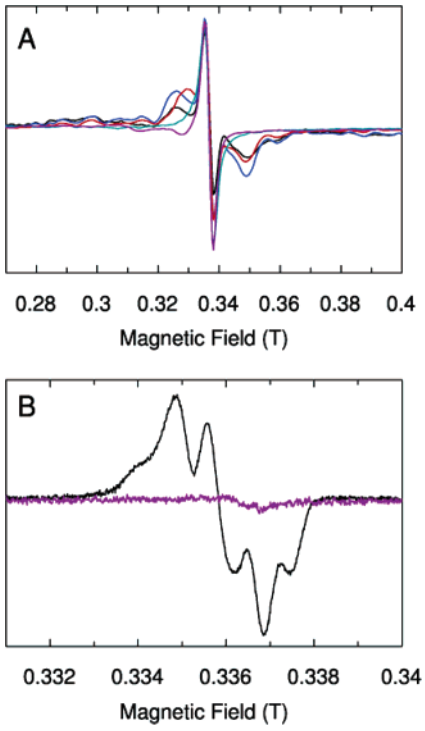

FIGURE 4: (A) EPR spectra (9 GHz) in acetate-treated D2-Tyr160Phe-PSII from *T. elongatus*. The light-minus-dark spectra were recorded at 4 (black), 8 (blue), 15 (red), 50 (green), and 116 K (violet). The chlorophyll concentration was ~1 mg/mL. Instrument settings were the same as in Figure 1. (B) EPR spectra (9 GHz) recorded at 116 K of the $Tyr_D^{\bullet}$ magnetic field region in the WT′ sample (black) and in illuminated acetate-treated D2-Tyr160Phe-PSII (violet). Instrument settings: modulation amplitude, 2.8 G; microwave power, 0.1 mW; microwave frequency, 9.4 GHz; and modulation frequency, 100 kHz.

inconsistent with the high-field data. Figure 4B shows the tyrosine radical region of the 9 GHz spectrum obtained at 116 K of an untreated dark-adapted WT′ PSII sample (black trace) and an illuminated acetate-treated D2-Tyr160Phe-PSII sample in which the split signal has been formed and can be detected at 8 K, but not at 116 K (violet trace). Both spectra have been normalized to the same reaction center concentration. These spectra show that no magnetically decoupled or uncoupled $Tyr^{\bullet}$ resonances are observable in the acetate-treated D2-Tyr160Phe-PSII sample at high temperatures. On this point, the 9 GHz and HFEPR data of the PSII sample from *T. elongatus* were completely consistent. Hence, it appears that the previously observed phenomenon

attributed to thermally induced magnetic decoupling is more likely due to the temperature-dependent relaxation that enhances the detection of $Tyr_D^{\bullet}$, since in the absence of $Tyr_D^{\bullet}$ no $Tyr^{\bullet}$ resonances are observed.

The temperature dependence of the 9 and 285 GHz spectra was not the same, but this was not totally unexpected. Spin dynamics and relaxation mechanisms are often field-dependent. For example, the dynamics of a two-site chemical exchange process depends on the absolute difference in the energies of the resonances of the two species that are involved. Hence, they will directly depend on the observation frequency. We have also experimentally observed in a crystalline sample of a Mn(III)Mn(IV) binuclear manganese complexes dynamical processes that are clearly different at 9 and 285 GHz (*41*). At the lower observation frequency, no temperature dependence was observed, while at higher observation frequencies, additional resonances, presumably arising from spin−spin couplings, were observed with an increase in temperature.

The complexity of the spin−spin interactions greatly complicated simulation strategies by requiring not only an adequate spin Hamiltonian but also a model for the distribution of spin−spin interactions. Although the approximate size of the coupling could be readily "read off" from the 9 GHz spectra, information about the radical itself was obscured. In fact, even in our study of the simpler plant signal, we were forced to fix the *g* values of the radical to reduce the complexity of the simulation. As we have shown previously, a multifrequency approach can greatly improve the situation. We decided to extend a direct measurement approach in which the resonant field positions of various spectral features are measured as a function of the microwave frequency. This approach permits the spin parameters, such as *g* values, to be directly determined and has been previously used to determine the *g* values of a mixed-valence binuclear manganese complex (*41*) and the manganese(II) centers in superoxide dismutases (*42*). The detailed theoretical basis for the method as applied to a $S_2Tyr_Z^{\bullet}$ spin-coupled pair is described in the Appendix.

The results of these field frequency measurements are shown in Figure 5 and summarized in Table 1. Data were obtained at eight different frequencies, four in the 190 GHz region (Figure 5, left panel) and another four in the 285 GHz region (Figure 5, right panel). Six different spectral features indicated in Figure 2 were measured. Five of the features were sharp peaks in the derivative spectrum, while the sixth was the high-field edge. For this high-field edge, we used the half-height in the derivative spectra. In each of the six cases, the eight resulting field frequency points were fit to a line. Due to the low signal-to-noise ratio and the broadness of the edge features, the precision of the measurement was much lower than that of the five peaks that were used and linear regression analysis yielded greater errors in fitting. Two of the monitored peaks, marked with black arrows in Figure 2, were from the narrow chlorophyll radical. In these cases, the *g* values determined from the linear regression should have been equal to the corresponding g_{eff} values. Table 1 shows this was indeed the case to within 5×10^{-4} in *g* (*33*). The accuracy of the method could also be seen in the frequency intercepts of the chlorophyll measurements which predicted a zero magnetic field line width of ~20 MHz or 70 mT which agrees remarkably well with the observed

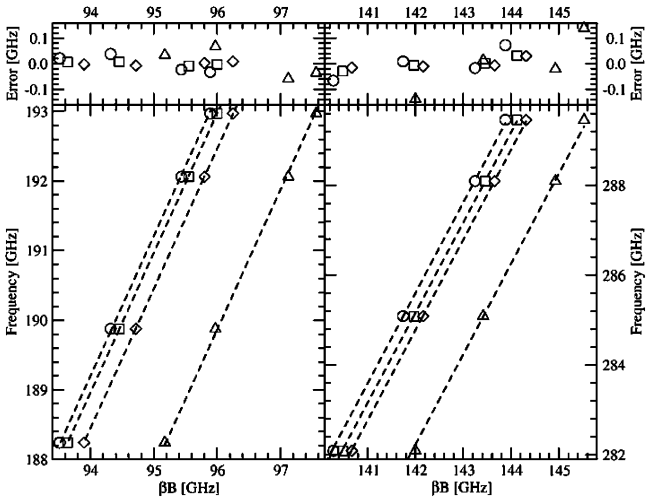

FIGURE 5: Field position of the resonances marked in Figure 2 as a function of the observation frequency. Although 190 and 285 GHz regions are shown separately, data from both regions were combined for the linear regression analysis, the results of which are summarized in Table 1. The same analysis was also carried out on the $Chl^{+\bullet}$ resonance but is not shown.

Table 1: Summary of the Linear Regression Analyses of Six Features in Split HFEPR Spectra Taken in the 190 and 285 GHz Frequency Regions[a]

g_{eff} at 285.09 GHz	intrinsic measured *g* value	error in *g* ($\times 10^{-4}$)	frequency intercept (GHz)	error in frequency intercept (GHz)
2.0111	2.00834	7.1	0.417	0.086
2.0082	2.00425	2.8	0.566	0.034
2.0054	2.00688	2.3	−0.200	0.028
1.9896	2.0079	13	−2.89	0.17
2.00232 ($chl^{\bullet+}$)	2.00277	2.1	−0.064	0.025
2.00302 ($chl^{\bullet+}$)	2.00338	2.5	−0.045	0.030

[a] The correlation coefficient in all cases was 1. g_{eff} is defined as $f/\beta B_r$, where *f* is the observation frequency and B_r is the measured magnetic-field position.

9 GHz line width of 90 mT once the 10 mT contribution from the *g* anisotropy is added to the zero-field width. The residuals for the three peaks, corresponding to the spin-coupled radical, were very small, less 0.01 GHz in both the 190 and 285 GHz regions. There appeared to be a slight trend in residuals noticeable in the 285 GHz data, indicating a small systematic deviation from linearity due to either measurement error, the nonlinear influence of the spin−spin coupling, or both. Nonetheless, the deviations were very small. This implied that the *g* values obtained from the slopes of the linear fits were well within 1×10^{-3} in *g* of the intrinsic values of the radical component.

The measured intrinsic *g* values of the two lowest-field resonances, marked with the green arrows in Figure 2, were lower than their g_{eff} values, indicating that the spin coupling in the centers corresponding to these resonances was antiferromagnetic ($C > 0$) while the coupling in the centers corresponding to the resonances with the g_{eff} of 2.0054 and the high-field edge of the spectra, both marked with the blue arrows in Figure 2, were ferromagnetic ($C < 0$). Similar to the control measurements on the chlorophyll radical, the zero-field intercepts of the five features gave an estimate of the size of the field-independent component to spectrum width which in these cases was presumably dominated by the spin−spin coupling. The zero-field intercepts of the three low-

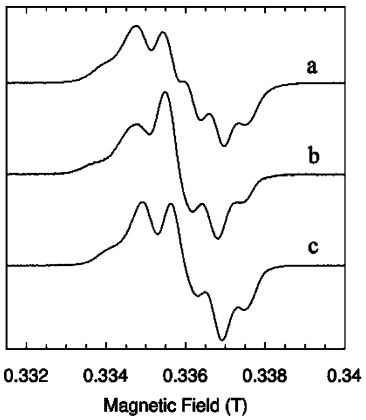

FIGURE 6: EPR signals (9 GHz) of $Tyr_D^{\bullet}$ and $Tyr_Z^{\bullet}$ in Mn-depleted D2-His189Leu-PSII. Spectrum a corresponds to $Tyr_Z^{\bullet}$, the part of the signal that disappears during the first minute of dark adaptation following the continuous illumination at −35 °C. Spectrum b was recorded after dark adaptation for 20 min at −35 °C and corresponds to $Tyr_D^{\bullet}$. Spectrum c is that of $Tyr_D^{\bullet}$ in WT′ PSII. Instrument settings: temperature, 15 K; modulation amplitude, 2.8 G; microwave power, 10 μW; microwave frequency, 9.4 GHz; and modulation frequency, 100 kHz. The amplitudes of the spectra have been arbitrarily scaled.

field resonances (g_{eff} = 2.0111, 2.0082, and 2.0054) were consistent with previously measured couplings for the split signal in acetate-treated and Ca^{2+}-depleted plant PSII samples (*34*). The zero-field intercept corresponding to the high-field edge of the spectrum was slightly below −3 GHz, indicating a spin coupling larger than that previously measured.

The difference in the two g_{eff} values for the antiferromagnetically coupled centers (g_{eff} = 2.0111 and 2.0082 with a Δg_{eff} of 0.0029) did not equal the corresponding difference in their intrinsic g values (Δg = 0.0041). The quantity $|\Delta g_{eff} - \Delta g|$ was ∼180 MHz. If one assumed that this difference was due to dipolar coupling, then the corresponding dipolar coupling constant was 120 MHz, the same value obtained from simulations of the HFEPR spectra of the $S_2Tyr_Z^{\bullet}$ state in acetate-treated plant PSII (*30*). Hence, we took this as direct evidence of the presence of dipolar spin−spin coupling and the approximate collinearity of the dipolar and **g** tensors.

In all four cases, the measured g values were entirely consistent with those of tyrosyl radicals. The measured g value of 2.00425 was assigned to the g_y value of the antiferromagnetically coupled centers since it was very close to the g_y values observed for all tyrosyl radicals (*33*), and since the spin−spin coupling and **g** tensors appear to be collinear, the corresponding g_x value for these centers was 2.0083. There were two possible interpretations for the ferromagnetic resonances corresponding to the intrinsic g values of 2.0079 and 2.0069. (1) They came from the same ferromagnetically coupled centers that had different orientations with respect to the magnetic field, or (2) they were from unrelated ferromagnetically coupled centers. The first possibility implied that the two centers had magnetic field orientations that were nearly orthogonal to each other since the resonances were close to the opposite extremes of the ferromagnetic portion of the spectrum. However, this was inconsistent with the closeness of the two values and the fact that the intrinsic g_y and g_z values were known to be 2.0045 and 2.0021 for all tyrosyl radicals (*33*). Hence, we favored the second possibility. The intrinsic g_x values of the two types of ferromagnetically coupled centers may have been in fact larger than the measured values depending on the orientation of the dipolar and **g** tensors. However, we assumed that the measured g values of 2.0079 and 2.0069 did indeed correspond to g_x values. This allowed us to consider a much broader range of possible g_x values and their implications.

To put this broad range of g_x values into context, we examined the EPR spectra of *T. elongatus* PSII tyrosyl radicals in electrostatic environments that we expected to be very different on the basis of previous measurements on PSII from other species. Of particular interest in this regard were the g values of $Tyr_D^{\bullet}$ in the absence of a hydrogen bond and under "strained" electrostatic conditions. It has been known from spectroscopic studies (*43*−*45*) and now from the crystallographic data (*9*, *10*) that $Tyr_D^{\bullet}$ is hydrogen bonded to His189 of the D2 subunit. In a mutant where D2-His189 is replaced with a leucine reside, $Tyr_D^{\bullet}$ would be presumably non-hydrogen-bonded. The 9 GHz EPR spectra of $Tyr_D^{\bullet}$ have been reported in such mutants both in *Synechocystis* PCC 6803 (*43*) and in *Chlamydomonas reinhardtii* (*46*). In both cases, a narrow 10 G resonance with no resolved proton hyperfine structure was detected. This has raised questions about the identity of the radical species that gives rise to this signal. For these reasons, we decided to construct a D2-His189Leu mutant in *T. elongatus*.

The activity of PSII purified from the D2-His189Leu *T. elongatus* mutant is comparable to that of WT′. The S_2 multiline EPR signal is also similar to that measured in WT′ in terms of both amplitude and shape (see the Supporting Information). However, the $Tyr_D^{\bullet}$ EPR resonance was much smaller (approximately 4% in the dark-adapted state and 8% after one flash) when compared to that of WT′ (see the Supporting Information). Therefore, in active centers, Tyr_D is predominantly reduced in the D2-His189Leu mutant in *T. elongatus*. To further study the EPR signals from the tyrosine radicals in this mutant, Mn depletion was carried out and PSII was resuspended at pH 10.

In this Mn-depleted D2-H189L sample, $Tyr_Z^{\bullet}$ and $Tyr_D^{\bullet}$ were first generated simultaneously by an illumination at −35 °C. The $Tyr^{\bullet}$ 9 GHz EPR signals were recorded at 15 K immediately after the illumination and after further dark times at −35 °C (spectra not shown). Approximately half of the light-induced $Tyr^{\bullet}$ signal decayed at −35 °C with a $t_{1/2}$ close to 40 s and the other half with a $t_{1/2}$ close to 20 min (not shown). The fast and slow phases were therefore expected to correspond to $Tyr_Z^{\bullet}$ and $Tyr_D^{\bullet}$, respectively. Spectrum a in Figure 6 is the spectrum that disappears in 1 min at −35 °C, and spectrum b is the spectrum recorded after dark adaptation for 20 min at −35 °C. These conclusions were strongly supported by the shape of the fast phase spectrum (Figure 6, spectrum a) that is identical to $Tyr_Z^{\bullet}$ in WT′ (not shown). The D2-His189Leu $Tyr_D^{\bullet}$ spectrum was distinct in both isotropic g value and shape from that of WT′ $Tyr_D^{\bullet}$ (Figure 6, spectrum c).

To better understand the spectroscopic differences in the 9 GHz EPR spectra, we also examined the HFEPR spectra of several tyrosyl radicals in *T. elongatus* PSII. This also allowed us to take advantage of the recent crystallographic structural data and newly developed molecular biological and quantum chemical methods to reexamine the relationship between the environment of tyrosyl radicals and their g values. In Figure 7, five different tyrosyl radical HFEPR spectra arising from the *T. elongatus* PSII sample are shown

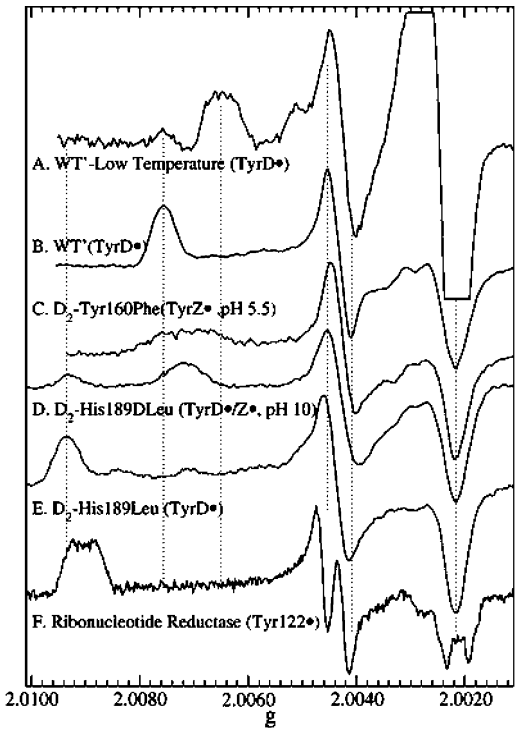

FIGURE 7: EPR spectra (285 GHz) of $Tyr_D^\bullet$ and $Tyr_Z^\bullet$ in Mn-depleted *T. elongatus* PSII. (A) WT′ $Tyr_D^\bullet$ induced in situ at 1.8 K by illumination for 20 min after dark adaptation for 4 h in the presence of 4 mM ferricyanide and 4 mM ferrocyanide at pH 8.5 [$Tyr_D^\bullet$ is reduced in the majority of centers under these conditions (*47*)]. (B) WT′ $Tyr_D^\bullet$ after dark adaptation for 5 min in the presence of 3 mM ferricyanide at pH 8.5. (C) $Tyr_Z^\bullet$ in the Mn-depleted D2-Tyr160Phe mutant induced by illumination for 5 s at −40 °C in the presence of 3 mM ferricyanide at pH 5.5 (acetate buffer). (D) $Tyr_D^\bullet$ and $Tyr_Z^\bullet$ in the Mn-depleted D2-His189Leu mutant induced by illumination for 5 s at pH 10. (E) D2-His189Leu-$Tyr_D^\bullet$ as for panel D after dark incubation for 5 min. (F) For reference, *E. coli* ribonucleotide reductase $Tyr122^\bullet$ is also shown.

along with the tyrosyl radical for *Escherichia coli* ribonucleotide reductase. As we have pointed out previously, the most remarkable features of the HFEPR spectra of these radicals are the large differences in their g_x values. The value of 2.0065 for the cryogenically photo-oxidized $Tyr_D^\bullet$ in WT′ *T. elongatus* PSII (Figure 7A) is one of lowest and is the same as that measured for PSII from spinach (*47*), while the value of 2.00934 for $Tyr_D^\bullet$ in the D2-His189Leu mutant is equal to that measured for the tyrosyl radical generated by the γ-irradiation of tyrosine in its neutral state (*48*). This high g_x value explains why even the 9 GHz spectrum of D2-His189Leu-$Tyr_D^\bullet$ was different from the wild-type resonance (Figure 6). It is also interesting to compare this value with the g_x value of $Tyr_D^\bullet$ in the *Synechocystis* PCC 6803 D2-His189Gln mutant that was found be 2.0083 (*44*). This range in values attests to the importance of the strength of histidine−tyrosine hydrogen bonding to the *g* values of the radical.

Two spectra of magnetically uncoupled $Tyr_Z^\bullet$ were obtained from samples in which the oxygen-evolving complex was removed. In one case, the radical was generated in the D2-Tyr160Phe mutant in pH 5.5 acetate buffer (Figure 7C). These conditions were similar to those used to generate the split signal described above. The other radical was formed in the D2-His189Leu mutant at pH 10 (Figure 7D). In *T. elongatus*, the g_x edge of $Tyr_Z^\bullet$ was considerably broader

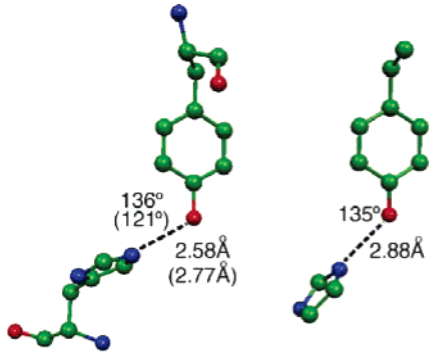

FIGURE 8: Comparison of the hydrogen bonding geometry of the $Tyr_D^\bullet$−His189 pair in PSII (left) and the B3LYP/6-31+G** geometry-optimized structure of an imidazole *p*-ethylphenoxy radical supercomplex in a 20 D dielectric medium (right). The values in parentheses are for the Tyr_Z−His190 pair. In the case of the $Tyr_D^\bullet$−His189 pair, the hydrogen bond donating imidazole nitrogen is rotated 30° relative to the phenoxy ring plane, while in the calculated complex and the Tyr_Z−His190 pair, it is in plane. The hydrogen atoms of the calculated structure are not shown for clarity. The values for PSII were taken from PDB entry 2AXT (*10*).

compared to that of $Tyr_D^\bullet$ as found previously in the *Synechocystis* PCC 6803 D2-Tyr160Phe mutant (*44*). However, the position of the edge was not the same as for $Tyr_D^\bullet$ (2.0076) as was the case in *Synechocystis* PCC 6803, but lower with a value of 2.0071. This value was also 0.0012 lower than that found for the split signal. The width of the g_x edge appeared to be pH-dependent, narrower at pH 10 than at pH 5 and 6. Further studies will need to be undertaken to determine whether these differences correspond to a titratable event.

These observed variations in the tyrosyl *g* values were put on a quantitative theoretical footing using computational methods available in Gaussian 03, as described above (*34*). In contrast to our previous report on similar calculations on amino acid radicals (*49*), we specifically addressed the specific role of hydrogen bonding in these calculations. The model system used was a *p*-ethylphenoxy−imidizole supramolecular complex. First, the structure of the supramolecular complex was globally optimized at the 6-31+G** level using the B3LYP density functional. The optimization was carried out in the presence of a medium with a dielectric constant of 20. The final geometry is shown in Figure 8. The optimized oxygen−proton distance was 1.86 Å with a corresponding g_x value of 2.0077. Both the *g* value and the hydrogen bonding distance were slightly greater than those determined experimentally for the $Tyr_D^\bullet$−His189 pair (*9*, *10*, *50*, *51*). The value for the isolated *p*-ethylphenoxy radical in the same 10 D medium was 2.0088, considerably lower than the experimental value of 2.0095 for the isolated radical. On the basis of the 2 and 5 D calculations, the g_x value of the isolated radical would be the same as that of the tyrosyl radical in the D2-His189Leu mutant in a 3 D medium.

The dependence of the *p*-ethylphenoxy g_x on the hydrogen bonding distance is shown in Figure 9. To determine how *g* values varied with hydrogen bonding distance, the globally optimized geometry was reoptimized with the phenoxy oxygen and hydrogen bond-donating imidizole nitrogen fixed at different distances. The angular geometry of the hydrogen bond was kept fixed. The g_x value at 10 Å was essentially that of the isolated *p*-ethylphenoxy radical.

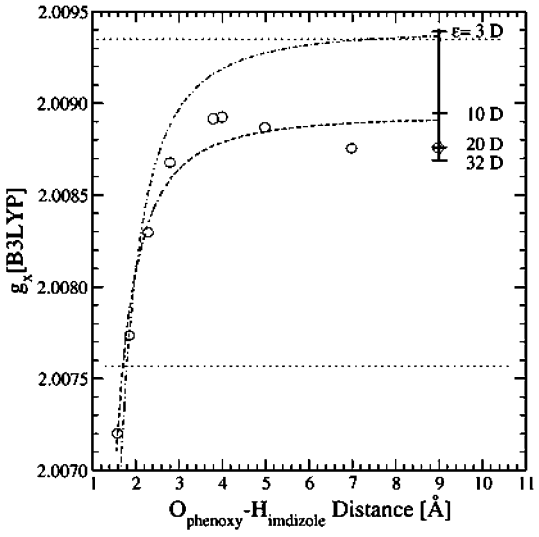

FIGURE 9: Dependence of calculated B3LYP/6-31+G** g_x values of the *p*-ethylphenoxy−imidizole supermolecular complex on the C−O···H−N hydrogen bonding distance (○). The dashed lines are functions of the form $g_x(r\rightarrow\infty) + S/(r - r_0)^2$, where r is the hydrogen bonding distance and $g_x(r\rightarrow\infty)$ is the asymptotic value. The physical significance of r_0 and the form of the function is explained in ref *44*. The function followed the calculated values best when $g_x(r\rightarrow\infty)$ was 2.00893, S was 0.00168, and r_0 was 0.601 (- - -). The dotted−dashed line for which $g_x(r\rightarrow\infty) = 2.0094$, $S = 0.00236$, and $r_0 = 0.665$ was determined by fitting the tyrosyl radical data from γ-irradiated ionic and molecular tyrosine crystals (*48*) and yeast ribonucleotide reductase (*52*, *60*). The vertical bar represents the range of calculated g_x values of the isolated *p*-ethylphenoxy radical in dielectric media ranging from 3 to 32 D. The 3 D data were interpolated from 2 and 5 D calculations.

DISCUSSION

These *ab initio* quantum chemical calculations again confirm that the g_x values of tyrosyl radicals are very sensitive to the immediate electronic structure of the protein environment. As we have noted before, the best computational results are obtained when not only the hydrogen bonding but also the local dielectric constant is explicitly taken into account (*49*). Such calculations are able to accurately reproduce the totality of the range of tyrosyl g_x values with the exception of the very low value (2.0065) observed for the cryogenically generated and trapped radical (*47*). Whether this reflects deficiencies in the computational method for determining g values or particularities in the radical−protein interactions that might be insufficiently modeled by our approach will need to be examined further. Qualitatively, the calculations clearly demonstrate that the cryogenically trapped state is very strained (Figure 7A). At the opposite extreme, the calculations indicate that the very high g_x value of the D2-His189Leu mutant must arise from the loss of the hydrogen bond and that the radical is in an electrostatically neutral environment. This is somewhat surprising since the crystallographic data indicate that D2-His189 in the wild type is likely to be hydrogen-bonded to the positively charged Arg294 (*9*, *10*). As is evident from the calculations and our previous work on mutants of ribonucleotide reductase (*52*), a positive charge even 8 Å from the radical should have had a measurable effect on the g_x value, yet the g_x value of 2.00934 for the D2-His189Leu mutant is the one of the highest values measured. Arg294 appears to have no effect, at least in the D2-His189Leu mutant. It is important to note that we cannot exclude other electrostatic interactions or interactions that have canceling effects, such as the presence of both electropositive and negative elements. The g_x value reflects the totality of the electrostatic environment that the tyrosyl radical "sees". Nonetheless, it is evident that when a leucine replaces His189, $Tyr_D^\bullet$ becomes strongly electrostatically insulated.

From the g_x values, the protein environment around *T. elongatus* $Tyr_Z^\bullet$ is apparently slightly different from that in plants (unpublished results) and *Synechocystis* PCC 6803 (*44*). In the Mn-depleted samples, all three radicals have a very broad g_x edge, which is most likely due to a distributed electrostatic environment arising from disordered hydrogen bond(s). The *T. elongatus* $Tyr_z^\bullet$ has an average g_x value that is slightly lower than that of $Tyr_D^\bullet$, while in the other two cases, their average g_x values are the same as that of $Tyr_D^\bullet$. The lower value of the *T. elongatus* radical indicates that it is in a slightly more electropositive environment than in the other two cases.

As we have discussed earlier, the disorder in hydrogen bonding may have been due to the removal of the nearby Mn_4Ca cluster and could have little significance in the intact centers (*44*). Nonetheless, even when the Mn_4Ca cluster is present, the $Tyr_Z^\bullet$ protein environment in *T. elongatus* appears to be very distributed and significantly different from that in plants. This conclusion comes from the fact that the HFEPR split signal is inherently different in the two cases. In the case of the plant protein, we have shown that the sign of the spin−spin coupling depends on the treatment used to generate the inhibited state, antiferromagnetic with calcium depletion and ferromagnetic with acetate. However, in the case of acetate-treated *T. elongatus* samples, it is clear from the HFEPR spectrum that the split signal arises from both antiferromagnetic and ferromagnetic centers. If one assumes that the intrinsic structure of the radical and Mn_4Ca cluster does not differ in spinach and *T. elongatus*, then the different signs of the spin−spin coupling must result from the protein surroundings that mediate the spin−spin coupling.

The measured g_x values of 2.00834 for the antiferromagnetic centers and 2.0069 and 2.0079 for ferromagnetic centers obtained from the field frequency measurements also indicated that the $Tyr_Z^\bullet$ protein environment about the two types of centers was likely to be different. The crystal structures suggest that $Tyr_Z^\bullet$ is hydrogen bonded by D1-His190 in an arrangement nearly identical to that of the BLY3P/6-31** geometry-optimized structure (Figure 8), with a hydrogen bonding distance of 2.77 Å from the nitrogen donor and oxygen acceptor and an angle of 121°. For $Tyr_Z^\bullet$ in centers lacking the nearby manganese cluster, the g_x value was 2.0071. Hence, the relatively high value in antiferromagnetic centers is somewhat curious since one might have expected the radical environment to be more electropositive in the proximity of both His190 and the positive metal ions of the Mn_4Ca cluster than in their absence. In fact, the same g value was measure for the g_x value of $Tyr_D^\bullet$ in the D2-His189Gln *Synechocystis* PCC 6803 mutant (*44*). At the time of those measurements, we had interpreted this high value as the loss of hydrogen bonding, but on the basis of our current state of knowledge, this value corresponds to a slightly electropositive surrounding or weak hydrogen bond. This is not inconsistent with vibrational spectroscopy mea-

surements (*53*). In the case of the radical in the $S_2Tyr_Z^\bullet$ state, one possible explanation might be that the positive charges of the metal ions are compensated by negatively charged ligands leading to a net neutral environment. By contrast, the two g_x values corresponding to the ferromagnetically coupled centers indicate an electropositive surrounding similar to $Tyr_Z^\bullet$ in the absence of the Mn_4Ca cluster. Moreover, since two different values were found, this strongly suggests that the ferromagnetically coupled population itself is heterogeneous. An interesting prospect is that the radical hydrogen bonding/electrostatic environment and the sign of the spin−spin coupling are related.

The two different types of spin-coupled centers also exhibited distinct temperature-dependent broadening. Apparently, the effect was greater for the antiferromagnetically coupled population since the high-field side more rapidly diminished in amplitude. From the experimental data, is was not possible to determine whether the effects were due to the dynamical effect of spin exchange or some other transversal spin relaxation (T_2) effects. What was clear was that up to temperatures greater than 100 K at both 9 and 285 GHz there was no evidence of any dynamical line narrowing or exchange narrowing. In a previous work, a narrow signal resembling that of an isolated tyrosyl radical was observed at high temperatures. Our work with the D2-Tyr160Phe mutant presented here would suggest that the narrow radical resonance was in fact due to $Tyr_D^\bullet$ which is known to have temperature-dependent relaxation properties (*54*, *55*).

The EPR measurements of the spin-coupled split-signal state in the D2-Tyr160Phe mutant also provided some additional structural insights. It has been established that the g_x axis of the tyrosyl radical **g** tensor corresponds to both phenoxyl C−O directions (*56*). Since the maximum in ferromagnetic spin−spin coupling (the feature with a g_{eff} value of 2.011) also corresponds to the intrinsic g_x value (2.00834) of $Tyr_Z^\bullet$, this would indicate that the C−O direction is collinear with the greatest spin−spin coupling direction. This would arise if the C−O bond were collinear with the dipolar axis, the vector connecting $Tyr_Z^\bullet$ and the Mn_4Ca cluster. This does not appear to be the case in the crystal structure, but a change in position, in particular, a rotation relative to the protein backbone, on oxidation cannot be excluded. We have argued that the tyrosyl radical in prostaglandin synthase undergoes such a rotation upon oxidation (*57*). Such a rotation might also reduce the hydrogen bonding contribution to the g_x value of $Tyr_Z^\bullet$, leading to the observed high value.

As we have seen, the *g* values of radicals can be measured directly even in the presence of spin−spin interactions, and it is possible to obtain detailed information regarding the radical and its interactions with the protein environment. We anticipate that this approach will be equally informative when it is applied to other PSII split signals that have been detected and other similar spin systems.

APPENDIX

Theoretical Basis for HFEPR Measurements. Much of the theory regarding EPR spectroscopy of the $S_2Tyr^\bullet$ split signal (*25*−*30*) and spin-coupled systems in general (*40*) has been discussed. Here we review the salient aspects that pertain to the measurements that we have made. The relevant spin Hamiltonian for the $S_2Tyr_Z^\bullet$ state is

$$H = \beta\vec{S}_R\cdot g_R\cdot\vec{B} + \beta\vec{S}_M\cdot g_M\cdot\vec{B} + \vec{S}_M\cdot\sum_i A_i\cdot\vec{I}_i + \vec{S}_R\cdot C\cdot\vec{S}_M \quad (1)$$

The first two terms are the Zeeman interactions of the radical and manganese cluster, respectively; the third is the four hyperfine interactions internal to the manganese cluster, and the last term is the general spin−spin coupling between the two spins. We neglect the radical hyperfine interactions. For our experiments at 6 and 10 T, the Zeeman interactions are 190 and 285 GHz, respectively, and from previous studies, the magnitude of the spin−spin coupling is known to be 300−800 MHz. Since the spin−spin interaction is much weaker than the Zeeman interaction, the spin−spin interaction can be treated as a perturbation. For the general case of two interacting spin $^1/_2$'s, Bencini and Gatteschi (*40*), following the earlier work of Smith and Pilbrow (*58*), have derived the energies of the four levels to second order. The four resulting EPR resonant field positions are given to first order by

$$B_i = \frac{h\nu}{g\beta} \pm \frac{C_{zz} - A(m_1,m_2,m_3,m_4)}{2g\beta} \pm \frac{\left\{\Lambda^2 + \frac{1}{4}[A(m_1,m_2,m_3,m_4) + \beta B_0(g_R - g_M)]^2\right\}^{1/2}}{g\beta} \quad \text{(I)}$$

where $g = (g_R + g_M)/2$, $g\beta B_0 = h\nu$, and

$$\Lambda^2 = \frac{1}{16}(C_{xx} + C_{yy})^2 + \frac{1}{16}(C_{yx} - C_{xy})^2$$

In the limit where there is no spin−spin interaction, eq I describes an EPR spectrum with two resonances at g_R and g_M. Although eq I is only to first order, the second-order terms are in fact very small. If one assumes a spin−spin coupling of 1 GHz, a value larger than that experimentally observed for the $S_2Tyr_Z^\bullet$ signal, then the second-order corrections to the energies are no larger than 10 MHz for an observation frequency of 190 GHz. This contribution is even smaller at 285 GHz. This means that eq I should accurately describe the resonant field positions to well within 1 part in 10^4. Nonetheless, even to first order, the resonant field positions will not be linearly dependent on the observation frequency due to the square-root term in eq I. Differentiation of the energy expressions that gives rise to eq I yields the following expression:

$$g_{app} = g_R \pm \frac{1}{2}\Delta g \times \left\{1 - \frac{1}{\sqrt{\left[\frac{\Lambda}{\beta B\Delta g - A(m_1,m_2,m_3,m_4)}\right]^2 + 1}}\right\} \quad \text{(II)}$$

where g_{eff} is the apparent *g* value of the radical with an intrinsic *g* value of g_R and Δg is $g_R - g_m$. It is important to note that g_{app} is not related to the commonly used g_{eff} [defined by $f/(g\beta B_{res})$, where *f* is the microwave frequency and B_{res} is the field position of the resonance in question] in a simple way and cannot be directly determined from a single spectrum, but rather, it must be measured from a series of spectra obtained at different frequencies. Equation II does

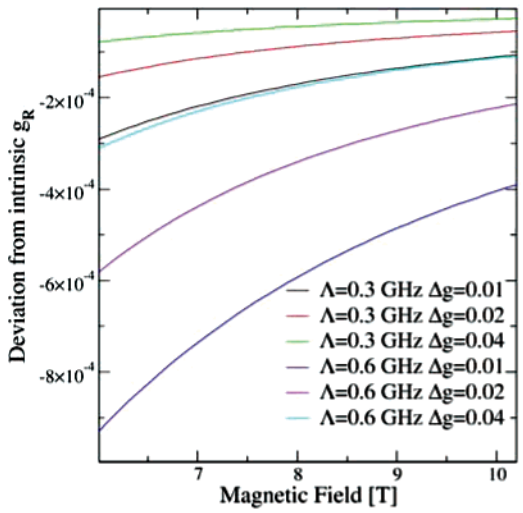

FIGURE 10: Deviation of g_{app} from g_R as a function of the magnetic field, the nonlinear coupling term, and Δg when $A(m_1,m_2,m_3,m_4)$ equals zero.

suggest that it should be possible to determine g_R by measuring how the resonant field position varies as a function of observation frequency.

Equation II indicates that the amount that the g_{app} of a radical will deviate from its intrinsic value, g_R, is determined by the ratio between the spin−spin coupling term Λ and the sum of the difference in Zeeman interactions and the total metal hyperfine interactions. In the particular case of the PSII manganese cluster, the metal hyperfine term depends on the nuclear spin quantum numbers and the hyperfine coupling constants for each of the four manganese nuclei. The g value of $Tyr_Z^\bullet$ ranges from ~2.01 to ~2.00, depending on its orientation with respect to the applied magnetic field (*44*). For the manganese cluster, g values have not been as well characterized but appear to be between 2.00 and 1.93. Various sets of hyperfine couplings for the S_2 multiline have been reported, but the couplings lie between 180 and 400 MHz (*30*, *59*). In the case where all four hyperfine couplings were the same and equal to a, there would be exactly 21 possible values for the hyperfine term ranging from $-10a$ to $10a$. The probability distribution of these values is just a binomial distribution. We have previously pointed out that the $A(m_1,m_2,m_3,m_4)$ term can be replaced by a continuous Gaussian function without strongly affecting the simulations (*30*). Apparently, the simulations are not sensitive to the details of the hyperfine couplings, but just to the sum of the couplings. Under the Gaussian or equal-couplings approximations, the most probable value of $A(m_1,m_2,m_3,m_4)$ is then zero, and we focus on this specific case.

Our previous simulations were calculated assuming a collinear **g** tensor and spin−spin coupling tensor model (*30*). We assumed that the g values of the radical were those of $Tyr_Z^\bullet$ in the absence of the manganese cluster and that the spin−spin coupling was composed of an isotropic exchange and anisotropic dipolar components. The total spin−spin coupling was found to range from 300 to 600 MHz depending on the specifics of the samples (*30*). For this model, Λ is then equal to $J + {}^1/_2D$ and the ratio of Δg to the total spin−spin coupling (the inverse of the fraction in eq II) when A is zero ranges from 0 ($\Delta g = 0$) to ~25 ($\Delta g = 0.08$) when the magnetic field is 7 T. At these two extremes, the resonant field positions of the radical given by eq I becomes linearly dependent on the observation frequency and g_{app} will be equal to g_R. Estimates of the intermediate cases can be numerically calculated and are shown in Figure 10 for the case in which $A(m_1,m_2,m_3,m_4)$ is zero. These curves show the difference between g_{app} and g_R for a variety of spin−spin couplings and Δg values. The effect of $A(m_1,m_2,m_3,m_4)$ is to give a shape to the resonance defined in eq I. For Gaussian-type hyperfine patterns, the line shape has a maximum where g_{app} and g_R are equal.

Figure 10 indicates that under ideal conditions it should be possible to directly determine the g values of a radical in a spin-coupled system to better than 1×10^{-3} in g by monitoring how the resonant field positions of the radical depend on the microwave frequency. Ideally, this relationship will be close to linear. The magnitude of the deviation from linearity will provide both an internal control of the measurement and information regarding the size of the spin−spin interaction with respect to Δg. It is expected that any systematic departure will be smaller at 10 T than at 6 T. We will refer to the experimental implementation of eq II as the "field frequency" method. This method is likely to be more robust for the purposes of measuring the g values of $Tyr_Z^\bullet$ in the $S_2Tyr_Z^\bullet$ state than approaches based on simulations that require accurate estimates of all of the terms of the spin Hamiltonian.

ACKNOWLEDGMENT

Le Centre de Calcul Recherche et Technologie (CCRT) of the CEA is acknowledged for access to Gaussian 03 and computational resources.

SUPPORTING INFORMATION AVAILABLE

EPR spectra relating to the formation of S_2 in WT′ and D2-His189Leu mutant PSII and $TyrD^\bullet$ in these proteins and the complete citation for ref *34*. This material is available free of charge via the Internet at http://pubs.acs.org.

REFERENCES

1. Diner, B. A. (2001) Amino acid residues involved in the coordination and assembly of the manganese cluster of photosystem II. Proton-coupled electron transport of the redox-active tyrosines and its relationship to water oxidation, *Biochim. Biophys. Acta 1503*, 147−163.
2. Debus, R. J. (2001) Amino acid residues that modulate the properties of tyrosine Y-Z and the manganese cluster in the water oxidizing complex of photosystem II, *Biochim. Biophys. Acta 1503*, 164−186.
3. McEvoy, J. P., and Brudvig, G. W. (2004) Structure-based mechanism of photosynthetic water oxidation, *Phys. Chem. Chem. Phys. 6*, 4754−4763.
4. Goussias, C., Boussac, A., and Rutherford, A. W. (2002) Photosystem II and photosynthetic oxidation of water: An overview, *Philos. Trans. R. Soc. London, Ser. B 357*, 1369−1381.
5. Rutherford, A. W., and Boussac, A. (2004) Water photolysis in biology, *Science 303*, 1782−1784.
6. Britt, R. D., Campbell, K. A., Peloquin, J. M., Gilchrist, M. L., Aznar, C. P., Dicus, M. M., Robblee, J., and Messinger, J. (2004) Recent pulsed EPR studies of the photosystem II oxygen-evolving complex: Implications as to water oxidation mechanisms, *Biochim. Biophys. Acta 1655*, 158−171.
7. Sauer, K., and Yachandra, V. K. (2004) The water-oxidation complex in photosynthesis, *Biochim. Biophys. Acta 1655*, 140−148.
8. Rutherford, A. W. (1989) Photosystem-II, the Water-Splitting Enzyme, *Trends Biochem. Sci. 14*, 227−232.

9. Ferreira, K. N., Iverson, T. M., Maghlaoui, K., Barber, J., and Iwata, S. (2004) Architecture of the photosynthetic oxygen-evolving center, *Science 303*, 1831−1838.
10. Loll, B., Kern, J., Saenger, W., Zouni, A., and Biesiadka, J. (2005) Towards complete cofactor arrangement in the 3.0 angstrom resolution structure of photosystem II, *Nature 438*, 1040−1044.
11. Yano, J., Kern, J., Irrgang, K. D., Latimer, M. J., Bergmann, U., Glatzel, P., Pushkar, Y., Biesiadka, J., Loll, B., Sauer, K., Messinger, J., Zouni, A., and Yachandra, V. K. (2005) X-ray damage to the Mn_4Ca complex in single crystals of photosystem II: A case study for metalloprotein crystallography, *Proc. Natl. Acad. Sci. U.S.A. 102*, 12047−12052.
12. Grabolle, M., Haumann, M., Muller, C., Liebisch, P., and Dau, H. (2006) Rapid loss of structural motifs in the manganese complex of oxygenic photosynthesis by X-ray irradiation at 10−300 K, *J. Biol. Chem. 281*, 4580−4588.
13. Sugiura, M., and Inoue, Y. (1999) Highly purified thermo-stable oxygen-evolving photosystem II core complex from the thermophilic cyanobacterium *Synechococcus elongatus* having His-tagged CP43, *Plant Cell Physiol. 40*, 1219−1231.
14. Nakamura, Y., Kaneko, T., Sato, S., Ikeuchi, M., Katoh, H., Sasamoto, S., Watanabe, A., Iriguchi, M., Kawashima, K., Kimura, T., Kishida, Y., Kiyokawa, C., Kohara, M., Matsumoto, M., Matsuno, A., Nakazaki, N., Shimpo, S., Sugimoto, M., Takeuchi, C., Yamada, M., and Tabata, S. (2002) Complete genome structure of the thermophilic cyanobacterium *Thermosynechococcus elongatus* BP-1, *DNA Res. 9*, 123−130.
15. Boussac, A., Sugiura, M., Inoue, Y., and Rutherford, A. W. (2000) EPR study of the oxygen evolving complex in His-tagged photosystem II from the cyanobacterium *Synechococcus elongatus*, *Biochemistry 39*, 13788−13799.
16. Sugiura, M., Rappaport, F., Brettel, K., Noguchi, T., Rutherford, A. W., and Boussac, A. (2004) Site-directed mutagenesis of the *Thermosynechococcus elongatus* photosystem II: The O-2-evolving enzyme lacking the redox-active tyrosine D, *Biochemistry 43*, 13549−13563.
17. Boussac, A., Zimmermann, J. L., and Rutherford, A. W. (1989) Epr Signals from Modified Charge Accumulation States of the Oxygen Evolving Enzyme in Ca^{2+}-Deficient Photosystem-II, *Biochemistry 28*, 8984−8989.
18. Boussac, A., Zimmermann, J. L., Rutherford, a. W., and Lavergne, J. (1990) Histidine Oxidation in the Oxygen-Evolving Photosystem-II Enzyme, *Nature 347*, 303−306.
19. Tang, X. S., Randall, D. W., Force, D. A., Diner, B. A., and Britt, R. D. (1996) Manganese-tyrosine interaction in the photosystem II oxygen-evolving complex, *J. Am. Chem. Soc. 118*, 7638−7639.
20. Mino, H., and Itoh, S. (2005) The origin of split EPR signals in the Ca^{2+}-depleted photosystem II, *Photosynth. Res. 84*, 333−337.
21. Petrouleas, V., Koulougliotis, D., and Ioannidis, N. (2005) Trapping of metalloradical intermediates of the S-states at liquid helium temperatures. Overview of the phenomenology and mechanistic implications, *Biochemistry 44*, 6723−6728.
22. Zhang, C., and Styring, S. (2003) Formation of split electron paramagnetic resonance signals in photosystem II suggests that $tyrosine_Z$ can be photooxidized at 5 K in the S_0 and S_1 states of the oxygen-evolving complex, *Biochemistry 42*, 8066−8076.
23. Zhang, C., Boussac, A., and Rutherford, A. W. (2004) Low-temperature electron transfer in photosystem II: A tyrosyl radical and semiquinone charge pair, *Biochemistry 43*, 13787−13795.
24. Boussac, A., Sugiura, M., Kirilovsky, D., and Rutherford, A. W. (2005) Near-infrared-induced transitions in the manganese cluster of photosystem II: Action spectra for the S_2 and S_3 redox states, *Plant Cell Physiol. 46*, 837−842.
25. Gilchrist, M. L., Ball, J. A., Randall, D. W., and Britt, R. D. (1995) Proximity of the Manganese Cluster of Photosystem-II to the Redox-Active Tyrosine Y-Z, *Proc. Natl. Acad. Sci. U.S.A. 92*, 9545−9549.
26. MacLachlan, D. J., Nugent, J. H. A., Warden, J. T., and Evans, M. C. W. (1994) Investigation of the Ammonium-Chloride and Ammonium Acetate Inhibition of Oxygen Evolution by Photosystem-II, *Biochim. Biophys. Acta 1188*, 325−334.
27. Force, D. A., Randall, D. W., and Britt, R. D. (1997) Proximity of acetate, manganese, and exchangeable deuterons to tyrosine $Y\text{-}Z^{\bullet}$ in acetate-inhibited photosystem II membranes: Implications for the direct involvement of $Y\text{-}Z^{\bullet}$ in water-splitting, *Biochemistry 36*, 12062−12070.
28. Dorlet, P., Di Valentin, M., Babcock, G. T., and McCracken, J. L. (1998) Interaction of Y-Z(center dot) with its environment in acetate-treated photosystem II membranes and reaction center cores, *J. Phys. Chem. B 102*, 8239−8247.
29. Lakshmi, K. V., Eaton, S. S., Eaton, G. R., Frank, H. A., and Brudvig, G. W. (1998) Analysis of dipolar and exchange interactions between manganese and tyrosine Z in the $S_2Y_Z^{\bullet}$ state of acetate-inhibited photosystem II via EPR spectral simulations at X- and Q-Bands, *J. Phys. Chem. B 102*, 8327−8335.
30. Dorlet, P., Boussac, A., Rutherford, A. W., and Un, S. (1999) Multifrequency high-field EPR study of the interaction between the tyrosyl Z radical and the manganese cluster in plant photosystem II, *J. Phys. Chem. B 103*, 10945−10954.
31. Kuhne, H., Szalai, V. A., and Brudvig, G. W. (1999) Competitive binding of acetate and chloride in photosystem II, *Biochemistry 38*, 6604−6613.
32. Szalai, V. A., Kuhne, H., Lakshmi, K. V., and Brudvig, G. W. (1998) Characterization of the interaction between manganese and tyrosine Z in acetate-inhibited photosystem II, *Biochemistry 37*, 13594−13603.
33. Un, S., Dorlet, P., and Rutherford, A. W. (2001) A high-field EPR tour of radicals in photosystems I and II, *Appl. Magn. Reson. 21*, 341−361.
34. Frisch, M. J., et al. (2003) *Gaussian 03*, Gaussian, Inc., Pittsburgh PA.
35. Becke, A. D. (1993) A New Mixing of Hartree-Fock and Local Density-Functional Theories, *J. Chem. Phys. 98*, 1372−1377.
36. Lee, C., Yang, W., and Parr, R. G. (1988) *Phys. Rev. B 37*, 785−789.
37. Stephens, P. J., Devlin, F. J., Chabalowski, C. F., and Frisch, M. J. (1994) Ab-Initio Calculation of Vibrational Absorption and Circular-Dichroism Spectra Using Density-Functional Force-Fields, *J. Phys. Chem. 98*, 11623−11627.
38. Neese, F. (2001) Prediction of electron paramagnetic resonance g values using coupled perturbed Hartree-Fock and Kohn-Sham theory, *J. Chem. Phys. 115*, 11080−11096.
39. Improta, R., and Barone, V. (2004) Interplay of electronic, environmental, and vibrational effects in determining the hyperfine coupling constants of organic free radicals, *Chem. Rev. 104*, 1231−1253.
40. Bencini, A., and Gatteschi, D. (1990) *Electron Paramagnetic Resonance of Exchange Coupled Systems*, Springer-Verlag, Berlin.
41. Hureau, C., Blondin, G., Cesario, M., and Un, S. (2003) Direct measurement of the hyperfine and *g*-tensors of a Mn(III)−Mn-(IV) complex in polycrystalline and frozen solution samples by high-field EPR, *J. Am. Chem. Soc. 125*, 11637−11645.
42. Un, S., Tabares, L. C., Cortez, N., Hiraoka, B. Y., and Yamakura, F. (2004) Manganese(II) zero-field interaction in cambialistic and manganese superoxide dismutases and its relationship to the structure of the metal binding site, *J. Am. Chem. Soc. 126*, 2720−2726.
43. Tang, X. S., Chisholm, D. A., Dismukes, G. C., Brudvig, G. W., and Diner, B. A. (1993) Spectroscopic Evidence from Site-Directed Mutants of *Synechocystis* PCC 6803 in Favor of a Close Interaction between Histidine-189 and Redox-Active Tyrosine-1608 Both of Polypeptide-D2 of the Photosystem-II Reaction-Center, *Biochemistry 32*, 13742−13748.
44. Un, S., Tang, X. S., and Diner, B. A. (1996) 245 GHz high-field EPR study of tyrosine-D zero and tyrosine-Z zero in mutants of photosystem II, *Biochemistry 35*, 679−684.
45. Campbell, K. A., Peloquin, J. M., Diner, B. A., Tang, X. S., Chisholm, D. A., and Britt, R. D. (1997) The τ-nitrogen of D2 histidine 189 is the hydrogen bond donor to the tyrosine radical $Y\text{-}D^{\bullet}$ of photosystem II, *J. Am. Chem. Soc. 119*, 4787−4788.
46. Tommos, C., Davidsson, L., Svensson, B., Madsen, C., Vermaas, W., and Styring, S. (1993) Modified EPR Spectra of the $Tyrosine_D$ Radical in Photosystem II in Site-Directed Mutants of *Synechocystis* sp. PCC 6803: Identification of Side Chains in the Immediate Vicinity of $Tyrosine_D$ on the D2 Protein, *Biochemistry 32*, 5436−5441.
47. Faller, P., Goussias, C., Rutherford, A. W., and Un, S. (2003) Resolving intermediates in biological proton-coupled electron transfer: A tyrosyl radical prior to proton movement, *Proc. Natl. Acad. Sci. U.S.A. 100*, 8732−8735.
48. Mezzetti, A., Maniero, A. L., Brustolon, M., Giacometti, G., and Brunel, L. C. (1999) A tyrosyl radical in an irradiated single crystal of N-acetyl-L-tyrosine studied by X-band cw-EPR, high-frequency EPR, and ENDOR spectroscopies, *J. Phys. Chem. A 103*, 9636−9643.

49. Un, S. (2005) The g-values and hyperfine coupling of amino acid radicals in proteins: Comparison of experimental measurements with ab initio calculations, *Magon. Reson. Chem. 43*, S229−S236.
50. Dorlet, P., Rutherford, A. W., and Un, S. (2000) Orientation of the tyrosyl D, pheophytin anion, and semiquinone $Q_A^{\bullet-}$ radicals in photosystem II determined by high-field electron paramagnetic resonance, *Biochemistry 39*, 7826−7834.
51. Hofbauer, W., Zouni, A., Bittl, R., Kern, J., Orth, P., Lendzian, F., Fromme, P., Witt, H. T., and Lubitz, W. (2001) Photosystem II single crystals studied by EPR spectroscopy at 94 GHz: The tyrosine radical Y-$D^{\bullet}$, *Proc. Natl. Acad. Sci. U.S.A. 98*, 6623−6628.
52. Un, S., Gerez, C., Elleingand, E., and Fontecave, M. (2001) Sensitivity of tyrosyl radical g-values to changes in protein structure: A high-field EPR study of mutants of ribonucleotide reductase, *J. Am. Chem. Soc. 123*, 3048−3054.
53. Berthomieu, C., and Hienerwadel, R. (2005) Vibrational spectroscopy to study the properties of redox-active tyrosines in photosystem II and other proteins, *Biochim. Biophys. Acta 1707*, 51−66.
54. Styring, S. A., and Rutherford, A. W. (1988) The microwave-power saturation of SI-slow varies with the redox state of the oxygen evolving complex in photosystem II, *Biochemistry 27*, 4915−4923.
55. Evelo, R. G., Styring, S. A., Rutherford, A. W., and Hoff, A. J. (1989) EPR relaxation measurements of photosystem II reaction centers: Influence of S-state oxidation and temperature, *Biochim. Biophys. Acta 973*, 428−442.
56. Fasanella, E. I., and Gordy, W. (1969) Electron Spin Resonance of an Irradiated Single Crystal of L-Tyrosine-Hc, *Proc. Natl. Acad. Sci. U.S.A. 62*, 299−304.
57. Dorlet, P., Seibold, S. A., Babcock, G. T., Gerfen, G. J., Smith, W. L., Tsai, A. L., and Un, S. (2002) High-field EPR study of tyrosyl radicals in prostaglandin H_2 synthase-1, *Biochemistry 41*, 6107−6114.
58. Smith, T. D., and Pilbrow, J. R. (1974) Determination of Structural-Properties of Dimeric Transition-Metal Ion Complexes from EPR-Spectra, *Coord. Chem. Rev. 13*, 173−278.
59. Peloquin, J. M., Campbell, K. A., Randall, D. W., Evanchik, M. A., Pecoraro, V. L., Armstrong, W. H., and Britt, R. D. (2000) Mn-55 ENDOR of the S_2-state multiline EPR signal of photosystem II: Implications on the structure of the tetranuclear Mn cluster, *J. Am. Chem. Soc. 122*, 10926−10942.
60. Bar, G., Bennati, M., Nguyen, H. H. T., Ge, J., Stubbe, J., and Griffin, R. G. (2001) High-frequency (140-GHz) time domain EPR and ENDOR spectroscopy: The tyrosyl radical-diiron cofactor in ribonucleotide reductase from yeast, *J. Am. Chem. Soc. 123*, 3569−3576.

BI062084F